

A battery-free smart mask for long-term exhaled breath biochemical sensing

Received: 7 August 2025

Accepted: 5 February 2026

Published online: 16 March 2026

 Check for updates

Wenzheng Heng^{1,7}, Christoph Putz^{2,3,7}, Wenying Tang^{1,4,7}, Jihong Min¹, Lukas E. Lehner^{2,3}, Stepan Demchyshyn^{2,3}, Gwangmook Kim^{2,3}, Canran Wang¹, Bekele Hailegnaw^{2,3}, Elias Rippatha⁵, Markus Scharber⁶, Moon-Ju Kim^{2,3}, Yonglin Chen^{2,3}, Zhiyong Fan⁴✉, Martin Kaltenbrunner^{2,3}✉ & Wei Gao¹✉

Exhaled breath condensate (EBC) offers a non-invasive window into respiratory and systemic metabolism, yet wearable EBC systems are constrained by unstable moisture harvesting, short sensor lifetimes in humidity and battery dependence. Here we present EBCLite, a battery-free smart mask for multiday EBC biomarker monitoring, using lactate as a model analyte. The platform integrates a regenerable antidrying porous hydrogel that achieves sustained and reactivatable breath condensation over several days, extending operational lifetime while reducing material cost. EBCLite further incorporates a long-term stable electrochemical lactate sensor and an ultrathin quasi-two-dimensional perovskite solar cell with a power-to-weight ratio of 10 W g^{-1} and a power conversion efficiency exceeding 30% under ambient indoor illumination, enabling autonomous operation across diverse lighting conditions. Human studies demonstrate strong correlations between EBC and blood lactate levels during exercise and carbohydrate intake, enabling real-time tracking of metabolic fluctuations. EBCLite provides a sustainable, user-friendly platform for continuous respiratory and metabolic monitoring.

Exhaled breath condensate (EBC) has emerged as a promising yet underutilized biofluid for non-invasive metabolic and respiratory health monitoring^{1,2}. Passively produced during normal respiration, EBC comprises water vapour and aerosolized droplets originating from the alveolar lining fluid and airway mucosa. These droplets contain a diverse array of volatile and non-volatile analytes^{3,4} (Fig. 1a) that reflect both local respiratory microenvironment and systemic physiological states, offering a non-invasive window into dynamic biochemical processes occurring deep in the lower respiratory tract. Conventional breath analysis has largely focused on gas-phase sensing of volatile

species (for example, O_2 , CO_2 and volatile organic compounds (VOCs)) using various detection modalities (Supplementary Table 1), which have established clinical and research utility but face well-documented challenges related to selectivity, humidity interference, long-term stability and miniaturization for continuous wear. Compared with other biofluids such as sweat, saliva and interstitial fluid, EBC collection is entirely passive, painless and stimulus-free, making it uniquely suitable for long-term and user-friendly health monitoring across diverse populations, including children, elderly individuals and critically ill patients⁵⁻⁷.

¹Andrew and Peggy Cherng Department of Medical Engineering, Division of Engineering and Applied Science, California Institute of Technology, Pasadena, CA, USA. ²Division of Soft Matter Physics, Institute of Experimental Physics, Johannes Kepler University Linz, Linz, Austria. ³Soft Materials Lab, Linz Institute of Technology, Johannes Kepler University Linz, Linz, Austria. ⁴Department of Electronic and Computer Engineering, The Hong Kong University of Science and Technology, Kowloon, China. ⁵Institute for Chemical Technology of Organic Materials, Johannes Kepler University Linz, Linz, Austria. ⁶Linz Institute for Organic Solar Cells, Johannes Kepler University Linz, Linz, Austria. ⁷These authors contributed equally: Wenzheng Heng, Christoph Putz, Wenying Tang. ✉e-mail: eezfan@ust.hk; martin.kaltenbrunner@jku.at; weigao@caltech.edu

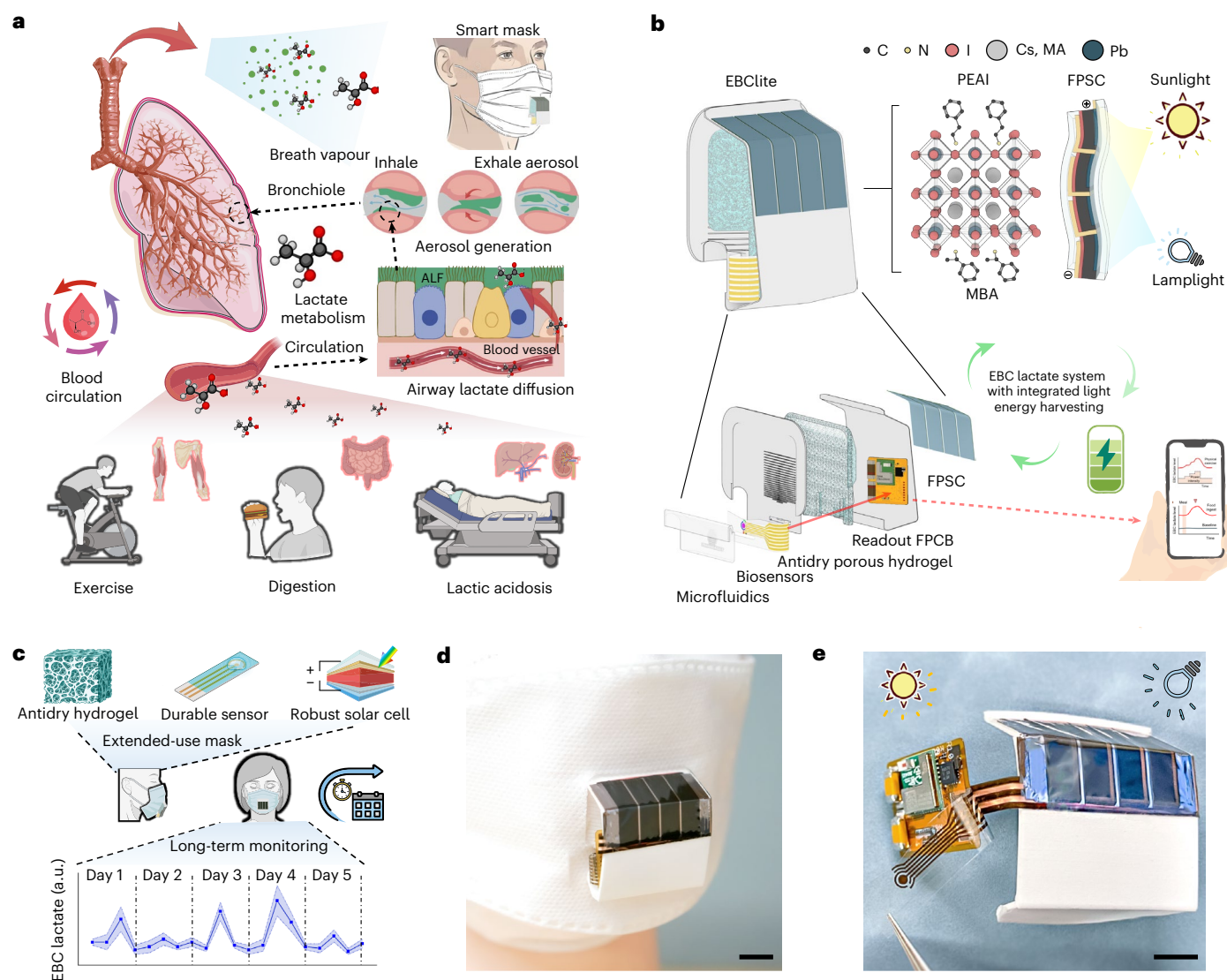


Fig. 1 | Overview of EBCLite for long-term sustained wireless exhaled breath metabolite monitoring. **a**, Schematic illustration of the origin and transport pathway of metabolites (for example, lactate) from blood to the airway surface liquid, where they diffuse across the epithelium and are incorporated into exhaled vapour before condensing as non-volatile metabolites in EBC. ALF, airway lining fluid. **b**, Schematic of the EBCLite platform integrating a regenerative hydrogel for breath condensation, a flexible electrochemical lactate sensor and an ultrathin perovskite solar module for continuous

wireless operation without external batteries. **c**, Long-duration on-body demonstration of the integrated EBCLite platform, showing stable hydrogel-assisted condensation, durable sensing and uninterrupted solar-powered operation over multiple days. **d**, Photograph of the fully assembled EBCLite smart mask with embedded perovskite solar module and biosensing array. Scale bar, 1 cm. **e**, Wireless EBCLite sensing electronics module powered by ambient light. Scale bar, 1 cm. Icons created in BioRender; Heng, W. <https://BioRender.com/d7rv27c> (2026).

Recent advances in wearable biosensors have opened the door for continuous biomolecular analysis of non-invasive biofluids^{8–10}. Wearable face masks^{11–14}—already part of daily life—offer a natural and ergonomic interface for EBC monitoring. When integrated with hydrogel-based cooling systems for condensate harvesting, they can passively collect breath moisture by lowering the local temperature below the dew point through evaporative cooling. Extending the operational lifespan of such smart mask systems could enable continuous and long-term biomarker tracking, enhance data completeness and reduce device turnover and costs (Supplementary Table 2). Matching the typical 3–5-day wear cycle of respirators such as N95 masks¹⁵ enhances the sustainability of smart mask deployment.

Despite the strong potential of masks for continuous breath health monitoring, long-term wearable EBC-based biochemical sensing remains constrained by several critical challenges that limit its clinical and diagnostic utility. Chief among these is sustained breath

condensation. Conventional evaporative substrates—particularly hydrogels—tend to dry out within hours¹⁶, undermining their cooling capability and reducing analyte capture efficiency. Furthermore, structural instability due to dehydration limits hydrogel reusability, thus hindering their suitability for continuous monitoring. In parallel, most electrochemical sensors exhibit signal drift and rapid performance degradation under the hot, humid and low-ionic-strength conditions of exhaled breath, which are characterized by a scarcity of dissolved salts, thereby hampering signal stability and compromising measurement accuracy over time¹⁷.

Powering such wearable systems presents another hurdle as conventional lithium-ion batteries add bulk, limit flexibility and require periodic recharging, making them incompatible with lightweight, extended-use systems^{18–20}. While alternative energy harvesters exist²¹, motion-based generators are ineffective during inactivity²², and thermo-electric devices are constrained by limited skin temperature gradients²³.

Emerging photovoltaic technologies, exemplified by perovskite solar cells (PSCs), offer low-cost alternatives to silicon and are particularly attractive for flexible and wearable electronics. PSCs stand out for their high power conversion efficiency (PCE) and exceptional performance in indoor energy harvesting, enabled by their tunable bandgap and strong spectral compatibility with ambient illumination^{24–29}. Their solution processability enables not just low-cost, scalable production competitive with other photovoltaic technologies even at smaller scales³⁰, but also ultrathin, flexible modules with high power-to-weight ratios, ideal for integration on curved surfaces such as face masks^{24,26,31}. However, traditional PSCs rely on brittle transparent conductive oxides (TCOs) and contain moisture-sensitive layers, such as the perovskite absorber and transport layers, which limit their durability and effectiveness in real-world wearable breath monitoring applications where both high humidity exposure and variable lighting are unavoidable^{32–34}.

To overcome these challenges, we report EBCLite (EBC system for extended lactate tracking with integrated solar energy harvesting)—a fully self-powered smart mask system for prolonged and sustainable multiday continuous EBC analysis (Fig. 1a,b and Supplementary Fig. 1). EBCLite integrates three key features: (1) a porous, rehydratable hydrogel that provides sustained and regenerable cooling for multiday EBC condensation; (2) a long-term stable electrochemical sensor array capable of accurate biomarker detection in humid, low-ionic-strength conditions; and (3) an ultrathin, TCO-free quasi-two-dimensional (2D) perovskite solar module that autonomously powers the system under both indoor and outdoor lighting without adding unnecessary bulk or rigidity that would cause discomfort when wearing the mask for prolonged periods of time. The solar module features a bent geometry for enhanced angular light capture and is engineered with large organic cations and an aluminium oxide (AlO_x)-coated substrate to ensure high mechanical flexibility and stability under the warm and humid microenvironment created during mask use. Together, these design elements enable consistent battery-free power generation and uninterrupted system operation for over 4 days under real-world conditions.

We selected lactate as a model biomarker for its pivotal role in both clinical and physiological contexts. As a key metabolic intermediate and stress indicator, lactate is implicated in critical conditions such as sepsis³⁵, cardiovascular disorders³⁶, cancer^{37,38} and lactic acidosis³⁹ (a serious condition arising from excessive lactate accumulation and impaired pH homeostasis). It is also widely used to assess exercise intensity⁴⁰, muscular fatigue⁴⁰, anaerobic threshold^{41,42} and metabolic efficiency^{43,44}. However, current lactate monitoring relies on invasive blood sampling and laboratory-based assays, limiting its utility for real-time tracking⁴⁵. While recent wearable sensors have explored lactate detection in sweat⁴⁶, saliva⁴⁷ and interstitial fluid⁴⁸, each presents challenges for continuous monitoring: saliva is prone to contamination, interstitial fluid extraction remains intrusive, and sweat requires stimulation⁴⁹. By contrast, EBC provides clean, passive and continuous access to respiratory and systemic biomarkers—provided moisture collection, sensing and power delivery can be sustained in a wearable form⁵⁰. Through real-world validation studies, including exercise and dietary intake, EBCLite demonstrated stable, accurate and continuous tracking of lactate dynamics using a single mask worn over multiple days. These results highlight its robustness, biochemical fidelity and translational utility, positioning EBCLite as a practical and sustainable platform for autonomous, long-term metabolic monitoring in everyday environments.

Self-powered EBCLite system for long-term sustainable EBC analysis

The EBCLite system integrates a suite of robust, stable and reusable modules (Fig. 1c,d) to enable multiday autonomous monitoring of biomarkers in EBC. At its core is an antidrying, shape-stable porous hydrogel that retains its structural and functional integrity during periods of non-use and supports rapid and sustained breath condensation

upon reactivation. This hydrogel can be reactivated with minimal water after prolonged downtime, eliminating the need for bulky external cooling sources. The collected condensate is routed via microfluidic channels to a sensing unit for real-time biochemical analysis¹.

The system also features a long-lasting and highly selective electrochemical lactate sensor that operates stably for over several days without recalibration. To ensure continuous operation without conventional batteries, EBCLite incorporates a flexible, TCO-free quasi-2D perovskite solar module with a bent geometry that maximize light harvesting across a wide range of incident angles in both indoor and outdoor environments (Fig. 1e). This solar module delivers reliable power to the system under ambient lighting conditions.

Power management and data acquisition of EBCLite are handled by a low-power flexible printed circuit board (FPCB), which integrates sensor driving, signal processing and Bluetooth low energy (BLE) communication. The system supports multimodal electrochemical measurements—including amperometry, potentiometric and impedance spectroscopy—along with real-time internal calibration, enabling truly autonomous and on-demand continuous metabolic monitoring.

Designed with user comfort and discretion in mind, the EBCLite system features a compact, lightweight and flexible form factor that fits seamlessly inside a face mask without interfering with natural respiration or movement. A custom embedded controller and a smartphone-linked application dynamically adjust power consumption according to ambient light conditions and real-time system activity. Bioelectronic data are internally calibrated and wirelessly transmitted to a smartphone app, providing intuitive, real-time visualization and remote tracking of lactate trends throughout daily life.

Porous rehydration-activated hydrogel for multiday EBC condensation

Evaporative cooling provides an energy-efficient strategy for EBC harvesting. In the EBCLite system, we developed a porous composite hydrogel based on polyacrylamide (PAM)/lithium chloride (LiCl) that enables multiday condensation with repeated transitions between active and downtime states through a rehydration-triggered cooling regeneration mechanism (Methods). PAM provides a mechanically robust and rehydratable hydrogel matrix, while LiCl functions as a hygroscopic agent that retains moisture and prevents full dehydration. By maintaining a non-evaporating layer of bound water through ion–dipole interactions with the polymer network, LiCl suppresses network collapse and cracking, thereby preserving softness and structural integrity over multiday use. To further enhance performance, a salt-templating method using NaCl particles was used to create a highly porous network, enabling long-lasting moisture capture and effective breath condensation without external refrigeration or material replacement (Fig. 2a).

The integration of LiCl within the crosslinked PAM network conferred both structural stability and high water retention (Fig. 2b,c), substantially reducing shrinkage and collapse during drying. Upon rehydration, the hydrogel rapidly recovered its original shape and mechanical integrity properties rarely observed in conventional physically crosslinked hydrogels, such as agarose or gelatin, which typically suffer from irreversible deformation or structural collapse upon drying. Furthermore, the residual hygroscopic effect of LiCl slowed water loss during drying periods, maintaining stable contact with the condensation interface and supporting repeated use.

Although LiCl's strong water retention enhances longevity, it suppresses evaporation and thereby limits the overall cooling efficiency (Supplementary Fig. 2). To resolve this trade-off, we spatially modulated the LiCl distribution via porous structuring within the hydrogel (Fig. 2d and Supplementary Fig. 3). By confining highly concentrated LiCl to localized microdomains, the overall water-to-salt ratio was increased, promoting continuous evaporation and enhancing evaporative cooling performance (Supplementary Fig. 4). In parallel, the

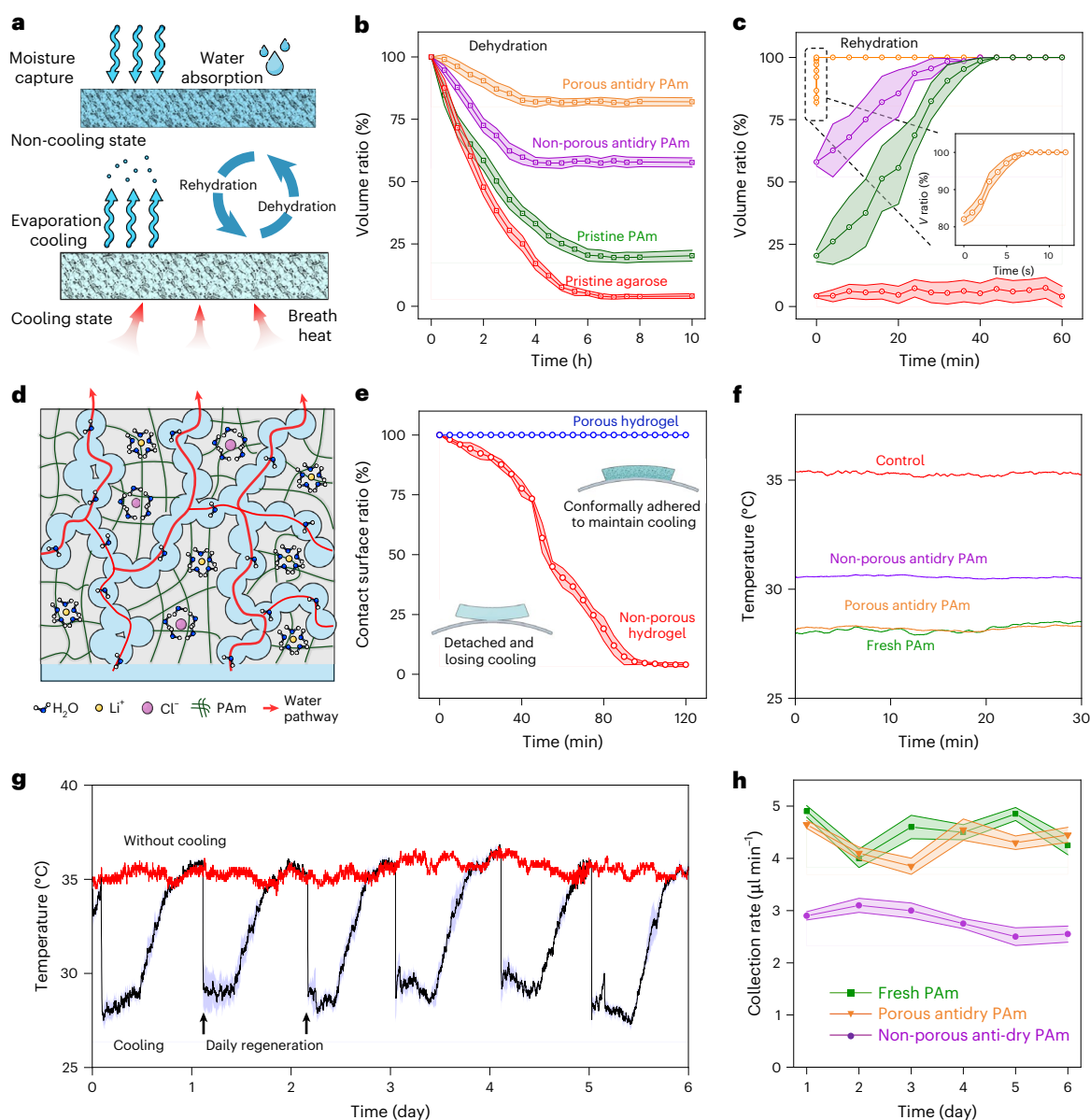


Fig. 2 | Porous antidry hydrogel for long-term evaporative cooling and EBC condensation. **a**, Hydration–dehydration cycle of the shape-retaining porous hydrogel. The hydrogel remains semi-dry yet structurally intact during storage and reactivates upon water addition to enable sustained evaporative cooling for EBC collection. **b**, Volume retention (mean \pm s.d.) comparison over 10 h showing enhanced antidrying and shape preservation in porous antidry PAm versus controls. **c**, Water uptake kinetics (mean \pm s.d.) highlighting rapid rehydration of porous hydrogels; inset shows volumetric expansion in the first 15 s ($n = 3$ tests). **d**, Structural schematic of the hydrogel's hierarchical architecture comprising

distributed ionic clusters LiCl, PAm and interconnected water channels. **e**, Surface adherence test (mean \pm s.d.) showing that porous hydrogels maintain contact with the device surface across all hydration states, unlike non-porous counterparts ($n = 3$ tests). **f**, Surface temperature profiles during evaporative cooling, confirming the enhanced cooling performance of porous hydrogels. **g**, Repeated temperature cycles (mean \pm s.d.) over 6 days confirm the stable cooling and durable performance of porous hydrogels under breath heating ($n = 3$ tests). **h**, Daily EBC collection rates (mean \pm s.d.) of a healthy participant over 6 days, with porous antidry PAm matching freshly prepared gel performance ($n = 3$ tests).

porous architecture alleviated evaporation-induced stress, preventing local warping and detachment at the thermal interface (Fig. 2e and Supplementary Fig. 5), while enhancing overall structural stability and conformal contact on curved surfaces to enhance heat dissipation¹ (Fig. 2f).

Notably, the LiCl-infused hydrogel demonstrated passive moisture absorption from ambient humidity in its non-cooling state, forming a self-regenerating water reservoir with extended operational longevity during storage (Supplementary Fig. 6). During six consecutive days of cyclic simulated breath condensation operation, the hydrogel consistently achieved a temperature reduction of approximately 7 °C per cycle (Fig. 2g). In addition, during the wearing EBC collection

test, the hydrogel maintained a high and stable condensation rate of 4–5 $\mu\text{l min}^{-1}$ across the 6-day test with minimal performance and morphology fluctuation, in stark contrast to the control group (pristine non-porous antidry hydrogel, $\sim 2.5 \mu\text{l min}^{-1}$) (Fig. 2h and Supplementary Fig. 7). These results confirm the hydrogel's robustness, reusability and suitability for continuous, on-demand cooling in wearable respiratory monitoring applications.

Flexible and durable sensor array for sustained EBC lactate monitoring

A key challenge for wearable electrochemical biosensors is their limited operational lifespan, particularly when exposed to complex

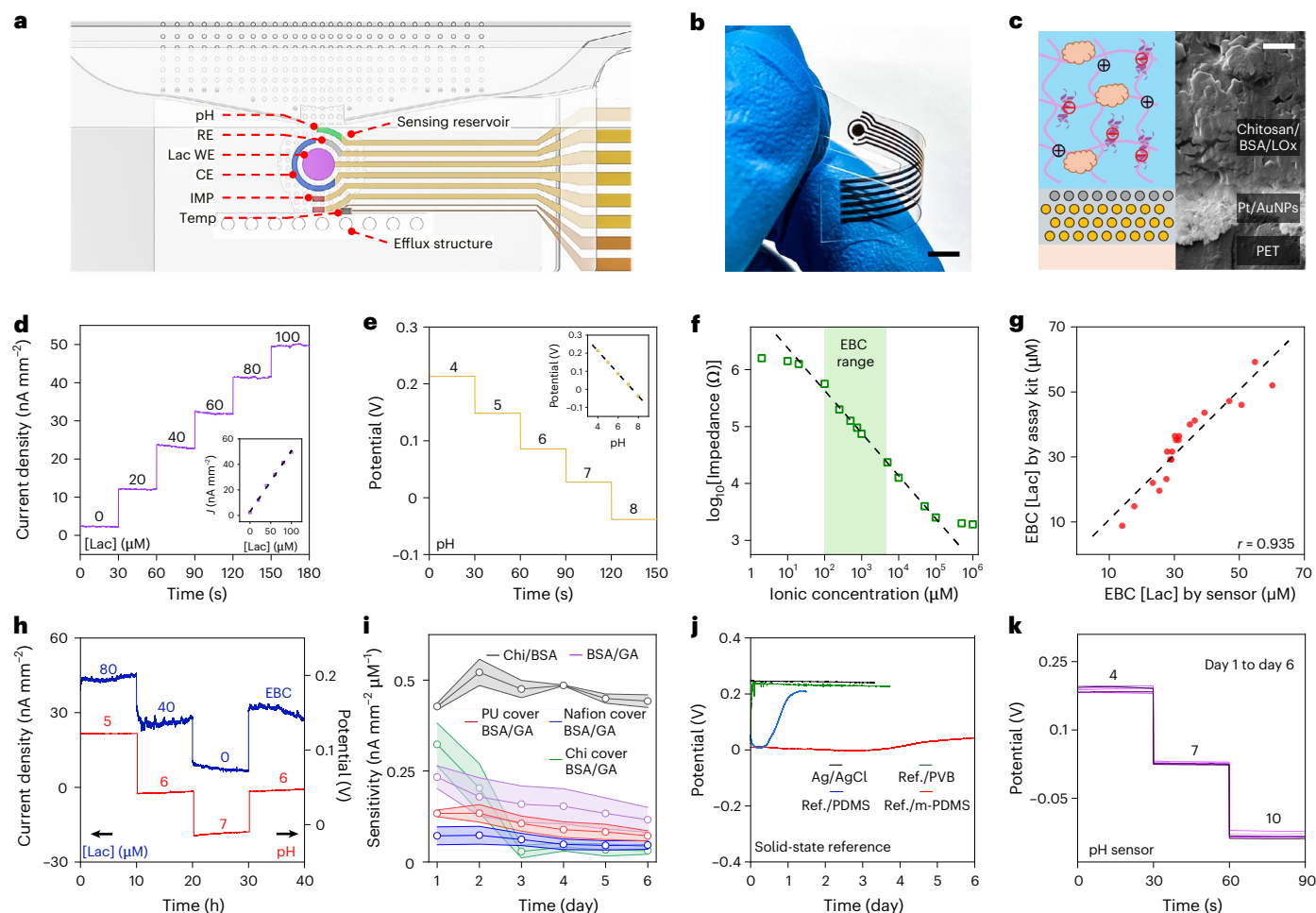


Fig. 3 | Flexible multisensor array for real-time prolonged EBC metabolic analysis. **a**, Schematic of the biosensor array comprising an enzymatic lactate sensor, a pH sensor, an impedance electrode-based ionic strength sensor and a resistive temperature sensor. Lac, lactate; WE, working electrode; RE, reference; CE, counter; IMP, impedance. **b**, Optical image of the flexible sensor array fabricated on a PET substrate. Scale bar, 3 mm. **c**, Scanning electron microscopy (SEM) image of the lactate sensor with enzyme-loaded biomatrix. Scale bar, 25 μm . AuNPs, gold nanoparticles. **d**, Amperometric response of the lactate sensor to physiologically relevant lactate concentrations. *J*, current density. **e**, Potentiometric response of the pH sensor across physiological pH ranges.

Insets: corresponding calibration curves. **f**, Impedimetric response of the ionic strength sensor measured across ionic strengths. **g**, Validation of the EBC lactate sensors against standard commercial assay kits. The Pearson correlation coefficient was acquired through linear regression ($n = 20$). **h**, Signal stability of lactate and pH sensors under 40-h continuous solution exposure. **i**, Sensitivity comparison (mean \pm s.d., $n = 3$) of encapsulation strategies under repeated wet-dry cycling. Chi, chitosan. **j**, Long-term stability of the solid-state reference electrode under 6-day continuous EBC exposure. m-PDMS, multilayer PDMS; Ref., Ag/AgCl. **k**, Day-to-day reproducibility of the pH measurements.

biological matrices. Moreover, repeated dry-wet cycling during prolonged use imposes additional stress on sensor integrity and signal stability. To achieve stable and accurate monitoring of EBC lactate, we developed a flexible biosensor array capable of withstanding repeated dry-wet cycles without substantial signal loss (Fig. 3a; for details of fabrication, see the Methods). The multimodal sensor array enables simultaneous detection of lactate, pH, ionic strength and temperature—key parameters for comprehensive EBC analysis. Importantly, its electrodes can be fabricated at scale via inkjet printing on a flexible polyethylene terephthalate (PET) substrate (Fig. 3b) with high device-to-device reproducibility and sensing performance (Supplementary Fig. 8).

The lactate-sensing electrode is embedded in a biocompatible hydrogel matrix composed of chitosan and bovine serum albumin (BSA), which maintains a hydrated microenvironment to preserve enzymatic activity and minimize signal drift (Fig. 3c). Chitosan's film-forming and proton-conductive properties, together with BSA's protein-stabilizing effect, enable long-term operational stability under humid, low-ionic-strength EBC conditions.

Under physiologically relevant conditions, the lactate sensor displayed a linear amperometric response across the biologically relevant range⁵⁰ (0–100 μM) with a sensitivity of $-0.5 \text{ nA } \mu\text{M}^{-1} \text{ mm}^{-2}$ (Fig. 3d) and the limit of quantification was $-1 \mu\text{M}$ (signal-to-noise ratio = 10; Supplementary Fig. 9). The pH sensor exhibited a near-Nernstian response across the EBC-relevant pH window (Fig. 3e), while the impedance-based ionic strength sensor showed a monotonic and log-linear response over typical ionic strengths in EBC (Fig. 3f). Together, these signals provide contextual information to enhance real-time calibration of lactate measurements (Supplementary Fig. 10).

Cross-reactivity tests confirmed the high selectivity of the lactate sensor against common breath-borne molecules (Supplementary Fig. 11). In addition, amperometric measurements with bare Pt electrodes showed negligible endogenous electroactive oxidants (including H_2O_2) in EBC, indicating minimal interference from background species. Selectivity is further enhanced by a permselective poly(*m*-phenylenediamine) (pPD) layer, which suppresses common electroactive interferents such as urate and ascorbic acid (Supplementary Fig. 11). Benchmarking against a commercial fluorescent assay using fresh

human EBC samples revealed a strong linear correlation (Pearson's $r = 0.935$) (Fig. 3g), confirming the system's quantitative reliability in real-sample analysis.

To assess long-term operational stability, lactate and pH sensors were tested continuously under simulated EBC conditions for ~40 h. Both maintained consistent signal amplitude and target response, supporting suitability for extended monitoring (Fig. 3h). To further enhance longevity, we systematically compared common enzyme immobilization and overlayer strategies (Fig. 3i). Across the immobilization strategies tested, all sensor films formed uniformly and displayed stable interfacial electrochemical behaviour under EBC conditions (Supplementary Figs. 12 and 13). However, the conventional glutaraldehyde (GA)-crosslinked BSA matrix, while initially responsive, exhibited rapid signal degradation after several days of repetitive wet-dry cycling (Fig. 3i). The addition of protective overlayers (for example, polyurethane (PU) and Nafion) offered only modest improvements and failed to preserve sensitivity over time. To assess the potential contribution of enzyme loss, we compared the concentration-response profiles of free and immobilized lactate oxidase (LOx) across varied enzyme loadings (Supplementary Fig. 14). Both systems showed parallel trends, suggesting that enzyme leaching was not the primary factor driving signal deterioration. Furthermore, LOx retained high activity in solution over 6 days, whereas sensors using the GA-BSA matrix exhibited progressive signal decline (Supplementary Fig. 15), consistent with chemical and conformational constraints imposed by GA crosslinking during the wet-dry test cycles^{51,52}. By contrast, a non-crosslinked chitosan/BSA composite matrix maintained high electrochemical sensitivity across 6 days of repeated use. This enhanced stability is probably due to the synergistic effects of chitosan's film-forming and proton-conductive properties and BSA's role in preserving enzyme conformation, together sustaining a hydrated microenvironment favourable for catalytic activity.

We also optimized the solid-state Ag/AgCl reference electrode by testing various encapsulation strategies (Fig. 3j). A multilayer polydimethylsiloxane (PDMS) encapsulation exhibited the best potential stability in EBC matrix over 6 days, maintaining performance under temperature, humidity and airflow perturbations and outperforming single-layer PDMS, polyvinyl butyral (PVB) coatings and unencapsulated versions (Supplementary Fig. 16). Its superior performance arises from enhanced mechanical flexibility, reducing electrolyte loss and preserving interface integrity (Supplementary Figs. 16 and 17). Additional tests confirmed long-term stability of the sensor array (Supplementary Fig. 18). When integrated with automated microfluidic channels, the complete sensing platform demonstrated robust performance and practicality (Supplementary Fig. 19).

FPSC-powered wireless system

To enable continuous, battery-free operation, we developed an ultrathin, flexible PSC (FPSC) module consisting of four 1-cm² cells in series (~4 cm² total active area) optimized for indoor and humid conditions (Fig. 4a and Supplementary Fig. 20). Built on a 6- μ m PET substrate with a 100-nm AlO₃ barrier layer and Cr/Au busbars, the FPSC utilizes poly(3,4-ethylenedioxythiophene)-poly(styrenesulfonate) (PEDOT:PSS) as the hole transport layer (HTL). The ~450-nm-thick absorber incorporates the bulky α -methylbenzylammonium (MBA) cation to facilitate the quasi-2D structure MBA₂(CS_{0.12}MA_{0.88})₆Pb₇I₂₂ resulting in large, micrometre-sized grains and effective defect passivation, thereby contributing to high performance and environmental stability²⁶ (Supplementary Fig. 21a). A thin layer of phenethylammonium iodide (PEAI) on top of the perovskite film forms an additional low-dimensional phase that improves energetic alignment, enhances radiative recombination, reduces interfacial trap densities and strengthens both mechanical resilience and device longevity^{26,53,54} (Supplementary Fig. 21b). Evaporated *N,N'*-dimethyl-3,4,9,10-perylenetetracarboxylic diimide (DiMe-PTCDI) and Cr/Au serve as the electron transport layer

(ETL) and top contacts, while a thin PU encapsulation layer positions it closer to the neutral mechanical plane²⁵ (Fig. 4b; for details of fabrication, see the Methods).

The module performs efficiently under both outdoor and indoor conditions (Fig. 4c). Under AM1.5 G solar simulation, the champion module achieved an open-circuit voltage (V_{oc}) of 4.46 V, a short-circuit current density (J_{sc}) of 4.9 mA cm⁻², a fill factor (FF) of 71% and a PCE of 15.5% (Supplementary Table 3). J - V stability of the module was confirmed by monitoring the voltage and current density at the MPP under AM1.5 G illumination, showing robust operational stability (Supplementary Fig. 22). Furthermore, the freestanding, PU-coated modules weigh 14.0 ± 0.4 g m⁻², achieving a specific power-per-weight of 10.0 ± 0.6 W g⁻¹. Critically, the module maintains high efficiency in low-light conditions. Indoor light sources, such as light-emitting diodes (LEDs), typically have a narrower emission spectrum compared with sunlight, which aligns well with the FPSC's external quantum efficiency (EQE) (Fig. 4d and Supplementary Fig. 23). In addition, the lower photon flux of indoor lighting reduces thermal and non-radiative losses⁵⁵. Under bright LED lighting conditions (4,000 K, 6,300 lx), the FPSC module achieved a PCE of 30.8%, and maintained 18.5% under 600 lx (Supplementary Fig. 24 and Supplementary Table 4). This exceptional indoor performance, nearly double the PCE observed under AM1.5 G illumination, is further supported by dark current measurements exhibiting low values at reverse bias, indicative of high film quality and minimal shunting pathways (Supplementary Fig. 24c).

As a reference, small-active area (0.16 cm²) single cells achieved a V_{oc}/J_{sc} , FF and PCE of 1.165 V, 21.5 mA cm⁻², 78% and 19.5% under AM1.5 G illumination (Supplementary Fig. 25 and Supplementary Table 3). Under indoor conditions (600 lx, 4,000 K LED), they exhibit a PCE of 29.2%, which increased to 35.4% under 6,100 lx, among the highest reported for ultrathin flexible indoor photovoltaics⁵⁶ (Supplementary Fig. 24 and Supplementary Table 2).

Notably, the module's power output scales reliably from dim to very bright lighting conditions (Fig. 4e). Even at 600 lx (4,000 K LED), the module provides continuous 150 μ W, enough to cover the system's average 100 μ W power consumption (Supplementary Table 5). In brief, the FPSC is markedly lighter (~11 mg), thinner (~8 μ m) and lower cost (US\$0.2 material cost, excluding labour cost) than coin cells while meeting the intended daytime use case; its output can be further increased simply by expanding active area, enabling higher power margins without compromising ergonomics.

Exploiting the module's flexibility, it can be bent sharply to form a 45° angle (Fig. 4a), broadening the range of incident angles available for efficient light harvesting. Compared with flat modules, this bent configuration substantially enhances the power output within a 115°–225° range, which are the typical incidence angles for ceiling-mounted lights, as recommended by industry guidelines EN 12464-1 and IES RP-1 (Fig. 4f and Supplementary Fig. 26).

Ambient stability was evaluated via maximum power point tracking (MPPT) of a freestanding, PU-coated, bent FPSC module at room temperature and 45–60% relative humidity (RH) under 6,000 lx LED light, retaining 80% of its power after 100 h (Fig. 4g, Supplementary Fig. 27 and Supplementary Table 6). Additional MPPT stability tests in high-humidity conditions (35 °C, 85% RH) were conducted to simulate the moisture-rich environment near the respiratory tract. Here, the PU coating proves insufficient for long-term operational stability, as it degrades several hours. Therefore, the module was coated with a thin layer of PDMS (70 \pm 5 μ m) to form an effective hydrophobic barrier (Supplementary Fig. 28). Under continuous illumination with 6,000 lx of 4,000-K LED light, the device retained 70% of its initial power output after 100 h, which remained sufficient to meet the system's average power demand (Fig. 4g and Supplementary Fig. 29). Furthermore, we confirmed the stability under real-world conditions by performing MPPT on a bent, freestanding, PDMS-coated module outdoors, in compliance with the International Summit on Organic Photovoltaic

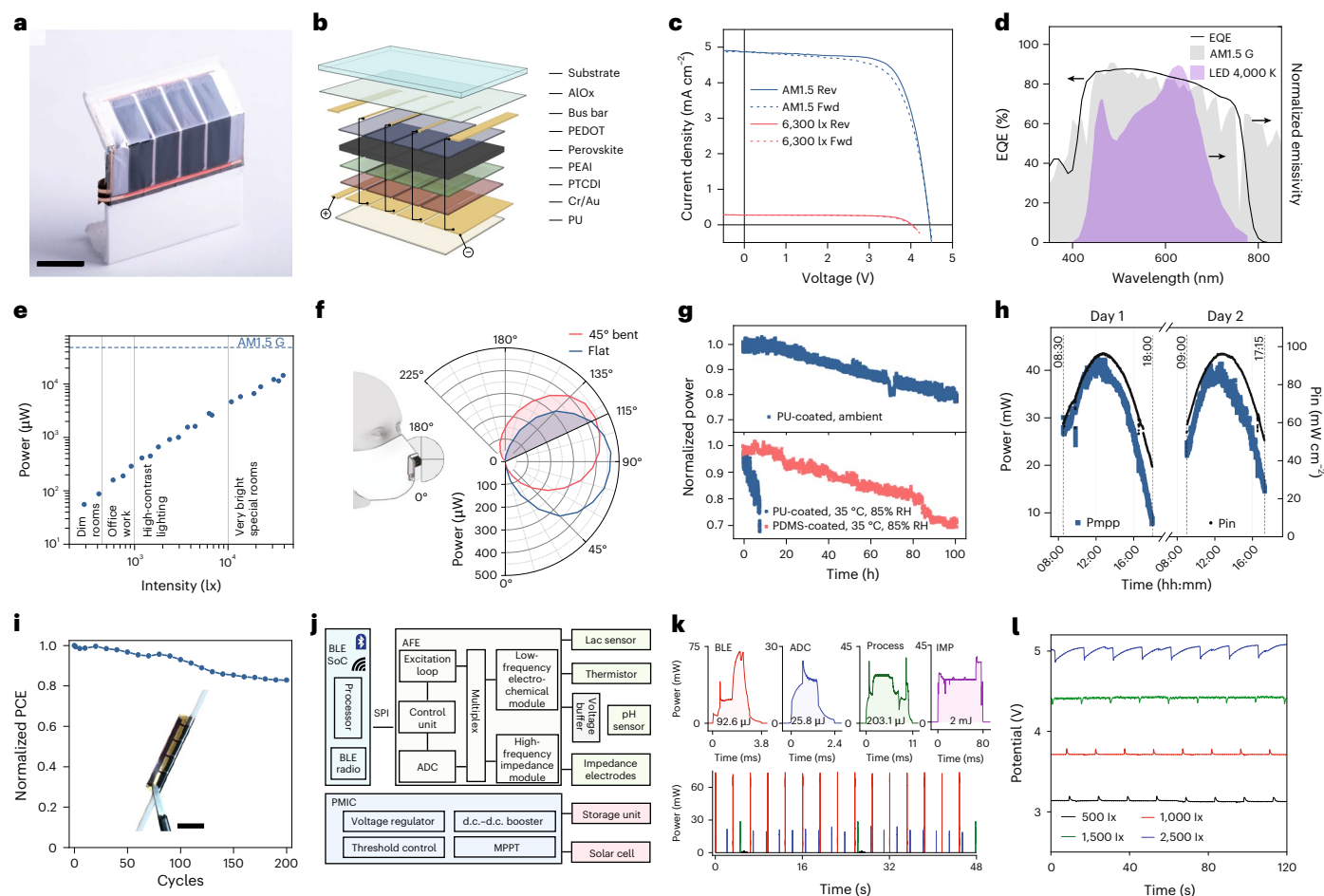


Fig. 4 | Design and characterization of the FPSC-powered system.

a, Photograph of the FPSC module. Scale bar, 1 cm. **b**, Three-dimensional model of the FPSC architecture with four series-connected cells ($\sim 1 \text{ cm}^2$ each). **c**, Reverse (Rev) and forward (Fwd) scanned $J-V$ curves recorded under AM1.5 G illumination and indoor LED light (4000 K, 6300 lx) at its highest PCE. **d**, EQE of the FPSC, superimposed with the normalized AM1.5 G and indoor LED (4,000 K) emission spectra. **e**, Power output of the FPSC as a function of illuminance. **f**, Polar plot showing the power output of flat (blue) and bent (red) FPSC configurations as a function of incident light angle (inset indicates light direction). Based on indoor lighting standards that limit the incident angle to 65° from vertical (marked as 115°), the bent configuration notably enhances power output over a broader angular range (115° – 225°) (LED 4,000 K, 1,300 lx). **g**, MPPT of a

PU-coated (blue) and PDMS-coated (red) bent, freestanding FPSCs under indoor LED light (4,000 K, 6,000 lx) for 100 h under ambient (top) and high-humidity (bottom) conditions. **h**, Outdoor MPPT conducted over 2 successive clear sunny days for a PDMS-coated freestanding, bent FPSC, with corresponding sunlight intensity. Pmpp, power at maximum power point; Pin, incident optical power. **i**, Normalized PCE of the FPSC as a function of 200 rolling cycles (1 mm radius). **j**, System-level block diagram of the integrated wearable device. SoC, system-on-chip; AFE, analogue front end; ADC, analogue-to-digital converter; Lac, lactate; SPI, Serial Peripheral Interface. **k**, Power profiling of key components averaging at a power of $\sim 100 \mu\text{W}$, well within the FPSC's indoor output. IMP, impedance measurement. **l**, Storage-unit voltage under 500–2,500 lx illumination.

Stability (ISOS) protocol (ISOS-O-3)⁵⁷. The test was conducted over 2 consecutive sunny days on a rooftop set-up, during which the device retained 71% of its initial power output, while enduring temperatures between 21°C and 33°C , RH levels between 25% and 50%, module temperatures as high as 45°C , and a peak solar irradiance of 95 mW cm^{-2} (Fig. 4h, Supplementary Fig. 30 and Supplementary Table 6).

By utilizing the ultrathin substrate, we developed highly flexible devices ~ 250 times thinner than traditional glass/indium tin oxide-based encapsulated PSCs. To assess their mechanical durability and simulate mask-flexing during wear, we measured PU-coated modules during repeated rolling around a rod (radius $\sim 1 \text{ mm}$; Fig. 4i and Supplementary Fig. 31). The modules retained over 90% of their initial performance after 100 cycles, and 82% after 200 cycles, confirming excellent mechanical resilience.

To efficiently manage power distribution, we developed a lightweight integrated circuit framework (Fig. 4j and Supplementary Figs. 32–34; Methods) that consolidates power management, sensor readout and communication modules. The system operates under a

duty-cycled sleep–wake scheme to minimize average consumption. The combined BLE, electrochemical and impedance modules collectively consume around $100 \mu\text{W}$ (ref. 24) (Supplementary Table 5), which remains well within the FPSC output even under low-illuminance conditions (Fig. 4k). An illumination–storage capacitor potential map (Fig. 4l) confirmed stable system operation across 500–2,500 lx, ensuring robust self-powered functionality in diverse lighting environments.

To validate EBCLite biocompatibility and safety for prolonged respiratory use (Methods), both intact and intentionally damaged FPSC modules were analysed for VOC release by gas chromatography. No VOCs were detected over 10 days of continuous monitoring (Supplementary Fig. 35), indicating no hazardous off-gassing under normal or failure modes. Simulated inhalation aerosol studies with inductively coupled plasma–mass spectrometry (ICP-MS) detected only trace Li^+ in collected aerosols—well below established toxicological thresholds⁵⁸—indicating negligible inhalation exposure during use (Supplementary Fig. 36). In parallel, Calu-3 cell assays revealed no significant differences in viability or morphology between control and

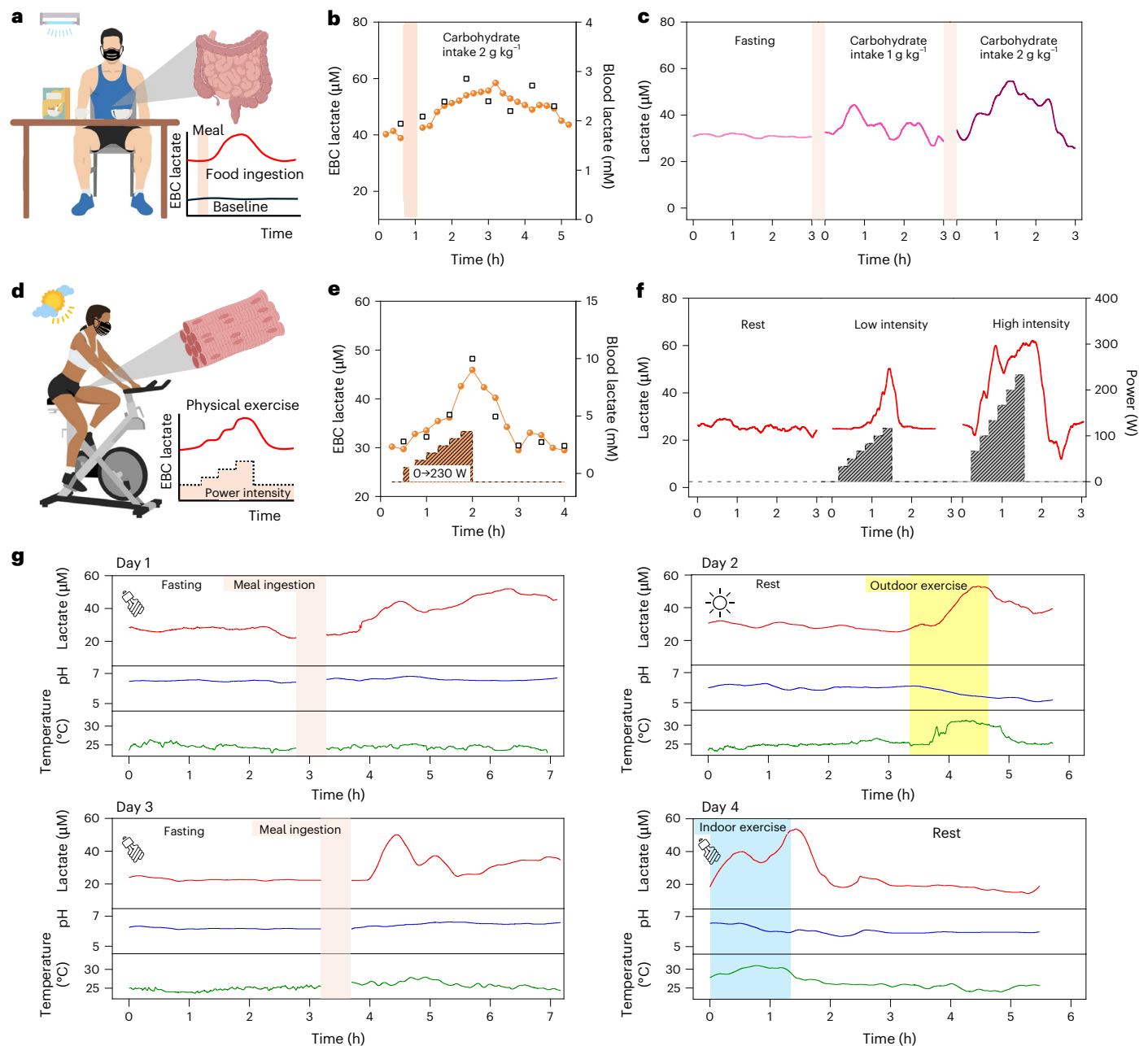


Fig. 5 | On-body validation of the EBCLite system for continuous metabolic tracking. **a**, Schematic of the carbohydrate ingestion protocol to induce postprandial lactate elevation. **b**, Time-course comparison of EBC and venous blood lactate showing strong temporal correlation over 4 h. Orange circular and black square markers indicate EBC and blood lactate concentrations, respectively. **c**, Dose-dependent EBC lactate response to 1 g kg^{-1} and 2 g kg^{-1} carbohydrate intake, indicating metabolic sensitivity. **d**, Illustration of graded cycling protocol to elicit intensity-dependent lactate production. **e**, EBC lactate

concentration measured at increasing exercise intensities. Orange circular and square markers indicate EBC and blood lactate concentrations, respectively. **f**, Real-time tracking of EBC lactate across rest, low-intensity exercise and high-intensity exercise stages, aligned with cycling power output. Grey-shaded areas represent distinct exercise intensities. **g**, Four-day continuous EBCLite monitoring of EBC lactate, pH and temperature during daily life, capturing metabolic responses to food, activity and rest. Icons created in BioRender; Heng, W. <https://BioRender.com/d7rv27c> (2026).

EBCLite-exposed groups over a 7-day culture period (Supplementary Fig. 37), confirming the system's biocompatibility.

In vivo validation of EBCLite for long-term metabolic monitoring

Lactate levels in blood rise transiently after carbohydrate intake or intense exercise owing to elevated glycolytic flux and a temporary imbalance between energy demand and oxidative capacity⁵⁹. A portion of circulating lactate is expelled via the lungs, allowing detection in EBC. To non-invasively track systemic lactate dynamics, we deployed

the EBCLite system for multiday studies involving dietary and exercise challenges (Supplementary Figs. 38 and 39).

Following oral carbohydrate intake under fasting conditions, EBC lactate levels increased in a time-dependent manner, mirroring blood lactate kinetics (Fig. 5a,b), and returned to baseline gradually over time as metabolic homeostasis was restored. Dose-response testing with 1 and 2 g kg^{-1} carbohydrate intake further confirmed the system's sensitivity, with both doses producing peak lactate ~ 2 h post-ingestion and dose-dependent differences clearly distinguished (Fig. 5c and Supplementary Figs. 40–42).

In the exercise challenge (Fig. 5d), exhaled lactate rose progressively with increasing workload. At low-intensities (0–100 W), lactate levels remained relatively stable, indicating predominantly aerobic metabolism. As workload increased (100–200 W), lactate began to rise, reflecting a shift to mixed aerobic–anaerobic metabolism. High-intensity exertion (>200 W) triggered a sharp lactate spike, signalling a transition to predominantly anaerobic metabolism due to insufficient oxygen supply and accelerated glycolysis. This intensity-stratified response highlights EBCLite's sensitivity in detecting real-time metabolic transitions during exercise. EBC and blood lactate profiles closely matched across all intensities (Fig. 5e and Supplementary Figs. 41 and 43), and the levels declined rapidly after exercise (Fig. 5f and Supplementary Fig. 43). Across an age heterogeneous, sex-balanced cohort ($n = 10$, 20–65 years old), on-body EBC lactate profiles were reproducible across sessions (Supplementary Table 7 and Supplementary Fig. 44), showed expected interindividual amplitude differences and broadly paralleled blood lactate, demonstrating the system's high temporal resolution to monitor rapid shifts in metabolic state.

During a continuous 4-day wear trial (Fig. 5g), EBCLite reliably tracked EBC lactate during daily activities, including exercise, meals and rest. Lactate levels rose rapidly after intense activity and gradually returned to baseline, while moderate increases followed food intake, demonstrating the system's sensitivity to routine metabolic fluctuations. Real-time pH and temperature readings enabled effective lactate signal calibration, ensuring consistent quantification under varying physiological conditions. These results confirm EBCLite's capability for continuous, long-term metabolic monitoring in real-world settings.

Meanwhile, the integrated FPSC maintained consistent uninterrupted power delivery across indoor and outdoor lighting conditions. On day 2, natural sunlight alone supported EBCLite's continuous outdoor operation, while lower ambient indoor lighting sufficed on other days. Together, these findings highlight the system's electrochemical stability, high temporal resolution and energy autonomy. Importantly, all functions were achieved using a single smart mask without any replacement of components or consumables, offering a low-cost, user-friendly platform for autonomous, long-term metabolic breath monitoring.

Conclusion

We present EBCLite, a self-powered smart mask system for continuous non-invasive EBC monitoring. By integrating a regenerative cooling hydrogel, a robust electrochemical lactate sensor and FPSCs, the system enables autonomous, long-term metabolic tracking without the need for batteries or consumables. The hydrogel facilitates sustained breath condensation with simple water addition to reactivation. The electrochemical sensor offers stable, multiday performance with high sensitivity, even under repeated dry–wet cycling. The perovskite solar module delivers reliable energy harvesting under humid and mechanically dynamic conditions, ensuring uninterrupted operation in real-world environments.

Validation studies confirmed that EBCLite accurately captures physiological lactate dynamics, including postprandial and exercise-induced fluctuations, with strong correlation to blood measurements. The system remained stable over a 4-day continuous wear test, demonstrating its suitability for daily health surveillance. By eliminating invasive sampling and power constraints, EBCLite establishes a new framework for sustainable, personalized respiratory biomonitoring and opens avenues for real-time, data-driven health interventions. Under this wearable framework, the detectable targets in EBC extend well beyond lactate. In principle, a wide spectrum of non-volatile biomarkers—including small-molecule metabolites (for example, acetone and lipids) as well as higher-order species such as proteins and pathogen-associated markers—can be quantified using established enzymatic or affinity-based transduction strategies (Supplementary Table 1).

Methods

Materials

Chloroplatinic acid hydrate, FeCl_3 and PbI_2 were purchased from Alfa Aesar. LiCl , PU and NaCl were from Thermo Fisher Scientific. Acrylamide, N,N,N',N' -tetramethylethylenediamine (TEMED), chitosan, BSA, N,N' -methylenebisacrylamide (MBAA), ammonium persulfate, Nafion (5 wt%), aniline, formic acid, lactic acid, NH_4HCO_3 , PbCl_2 , hydroiodic acid, α -methylbenzylamine, PEAL, CsI, N,N -dimethylformamide (DMF), chlorobenzene and chloroform were obtained from Sigma-Aldrich. Hexane, dimethyl sulfoxide (DMSO), acetone and isopropanol (IPA) were supplied by VWR Chemicals, and methylamine by Acros Organics. Gold ink (10 wt%) and silver ink were from C-INK and PV Nano Cell, respectively. SU-8 photoresist (Kayaku Advanced Materials), PDMS (Sylgard 184) and silicone adhesive MG2401 (Dow Corning), silver nanoparticles (SkySpring Nanomaterials), alumina microspheres (Meiqi Industrial), PET films (McMaster-Carr), PDMS-b-PEG block copolymers (SPECIFIC POLYMERS) and medical adhesive tapes (Adhesives Research) were used as substrates or supports. PEDOT:PSS (Clevios PH1000, Heraeus), ZonylFS-300 (Abcr), PU spray resin (Urethan 71, CRC Kontakt Chemie), Hellmanex III (Hellma Analytics), parylene-C dimer (Diener electronic), DiMe-PTCDI (Hoechst), Cr targets (Kurt J. Lesker) and Au pellets (Junker Edelmetalle) were used for device fabrication. EnzyChrom ammonia/ammonium assay kits (BioAssay Systems) and LOx (Toyobo) were used for biochemical analyses. Methylammonium iodide ($\text{CH}_3\text{NH}_3\text{I}$) and α -methylbenzylammonium iodide ($\text{C}_8\text{H}_9\text{NH}_3\text{I}$) were synthesized following a previously published procedure^{26,60}.

Preparation of porous LiClPAm hydrogel

Porous PAm hydrogels were prepared via a salt-leaching method using NaCl crystals (100–300 μm) as sacrificial porogens. Acrylamide (10–20 wt%) and MBAA (0.1–1 mol% relative to acrylamide) were dissolved in water, followed by ammonium persulfate (0.05–0.1 wt%) and TEMED (0.05–0.1 vol%) as redox initiators. The NaCl crystals were mixed with the precursor solution at a salt-to-polymer weight ratio of 8:1, and the mixture was cast into moulds and cured at room temperature for 5 min. After polymerization, the gels were immersed in deionized water for 24 h to remove the salt. The resulting hydrogels exhibited an interconnected porous structure, with pore size and porosity tunable by adjusting the size and content of NaCl particles⁶¹.

After desalting, the hydrogels were soaked in aqueous LiCl solution (0–40 wt%) for 12–24 h to enhance hygroscopicity and water retention. The concentration of LiCl served as a tunable parameter to modulate the hydrogel's moisture-holding capacity and evaporative cooling performance. Residual surface electrolyte was removed by gently pressing the gels against filter paper, ensuring hydration within the hydrogel matrix while keeping the pores unfilled.

Hydrogel cooling characterization

Hydrogel discs (2 mm thick, $\sim 5 \text{ cm}^2$ area) were mounted on a microstructured support layer (2.5 \times 3 cm, 0.5 mm thick) containing embedded microfluidic channels for potential water replenishment. The support was fabricated as part of the EBCLite system. To simulate breath-to-device heat exchange, a benchtop thermal platform was constructed using a Kapton heater (280 mW) mounted on a copper sheet for uniform heat distribution and embedded in a polystyrene foam base with aluminium foil insulation. A K-type thermocouple was placed at the hydrogel interface and connected to a data acquisition system (COMPAQ DAQ, Flux Teq), while heater power was controlled via a programmable power supply (Keithley 2231A-30-3). The cooling performance was quantified by the temperature differential (ΔT) between hydrogel-coated and uncoated modules. Evaporation rates were determined gravimetrically by monitoring mass loss at ~ 20 -min intervals. All experiments were conducted in a custom temperature–humidity chamber with precise control of ambient conditions and airflow.

Hydrogel dehydration and rehydration kinetics

To evaluate dynamic hydration behaviour, hydrogel samples were subjected to controlled dehydration and rehydration cycles under constant thermal flux. During the dehydration phase, the Kapton heater operated at a fixed power without external simulate EBC (sEBC) replenishment, allowing spontaneous water loss to proceed under steady-state heating. In the rehydration phase, sufficient water was introduced to enable full reswelling of the hydrogel. Throughout both phases, morphological changes were continuously recorded using a fixed-position camera. Hydrogel volume and contact area dynamics were quantified by image analysis, allowing extraction of projected contact area ratio and relative thickness changes over time.

Multiday cooling performance of hydrogel

Before each long-term condensation test, the porous hydrogel was rehydrated with a saturating volume of water to restore evaporative-cooling capacity. For benchtop thermal measurements, a syringe pump delivered quantified sEBC ($5 \mu\text{l min}^{-1}$) as make-up water.

During human wearing test use, participants wore the hydrogel-integrated EBCLite under varied environmental conditions. Nasal breathing was performed in an upright seated posture, and the device efflux port was sealed with PDMS to prevent EBC fluid loss. Condensate accumulated in the microfluidic layer was withdrawn every 20 min with a pipette and quantified gravimetrically. Unless otherwise specified, all trials were conducted by the same healthy participant to minimize interparticipant variability. 'Freshly prepared PAm' refers to a bulk, non-porous PAm hydrogel that has just been removed from water and remains in a fully hydrated, water-saturated state.

Sensor fabrication

Inkjet-printed electrode fabrication. Multimodal sensor patches were fabricated on PET substrates using an inkjet printer (DMP-2850, Fujifilm) via sequential printing of gold (for counter, pH, impedance and lactate sensors), silver (for reference electrode) and SU-8 (for encapsulation). Gold electrodes were printed at 40°C to accelerate solvent evaporation, followed by thermal sintering at 120°C for 2 h. Sensor outlines and fluidic inlets were defined using laser cutting.

Biosensor preparation. The Ag/AgCl reference electrode was fabricated by chlorinating a printed silver electrode via drop-casting of 0.1 M FeCl_3 . A solid-state reference membrane was subsequently formed by depositing a methanolic solution containing PVB and fine NaCl particles, followed by encapsulation with multiple layers of PDMS ($-0.5 \mu\text{l}$ per layer for a 1-mm-diameter electrode) and curing at 60°C . The process was repeated after each curing step to build up multiple layers. For enhanced stability, electrodes can be preconditioned in electrolyte solution to reach a stable potential. Alternatively, for rapid activation, microscale perforations can be introduced into the PDMS layer using microneedles to facilitate hydration.

The pH sensor was constructed by electrodepositing a polyaniline film on inkjet-printed gold electrodes via cyclic voltammetry (-0.2 V to 1.0 V , 50 mV s^{-1} , 20 cycles).

The lactate sensor was prepared by first electrodepositing platinum nanoparticles (PtNPs) onto gold electrodes (-0.1 V , 30 s) in an aqueous solution of $5\text{ mM H}_2\text{PtCl}_6$ and 1.5 mM formic acid. Optionally, a thin permselective pPD film was formed by electropolymerization on the PtNPs, holding $+0.60\text{ V}$ in 5 mM *m*-phenylenediamine monomer (0.1 M phosphate-buffered saline) solution for 600 s to suppress electroactive interferents. An enzymatic recognition layer was then formed by drop-casting $0.5 \mu\text{l}$ of a mixed solution comprising $1\text{ wt}\%$ chitosan (in 0.1 M acetic acid), 40 mg ml^{-1} LOx and 10 mg ml^{-1} BSA (in phosphate-buffered saline).

Biosensor characterization. For characterization of the pH sensors, McIlvaine buffers with pH values ranging from 4 to 8 were used.

For characterization of the lactate sensors, lactate solutions were prepared in sEBC buffer ($400\text{ }\mu\text{M NaHCO}_3$) with a pH of 6. Solid-state reference electrodes were characterized in KCl solutions of varying concentration and monitored in deionized water to assess long-term drift. The impedance sensor was calibrated using NaHCO_3 solutions of different concentrations to cover the ionic-strength range relevant to EBC. For the characterization of the sensors' dependence on temperature, a ceramic hot plate (Thermo Fisher Scientific) was used. For in vitro flow tests, a syringe pump (78-01001, Thermo Fisher Scientific) was used to inject various fluids through the microfluidic sensor patch at a constant flow rate ($5 \mu\text{l min}^{-1}$). Selectivity was assessed in three experiments. First, step chronoamperometry with chitosan/BSA/LOx/PtNPs electrodes applied lactate pulses interleaved with typical interferents to compare response order and magnitude. Second, the H_2O_2 -mediated pathway was validated on bare PtNPs by dosing EBC and incremental H_2O_2 and recording current steps to assess electroactive interference. Third, chitosan/BSA/LOx/PtNPs/pPD electrodes were used under equimolar challenges to derive quantitative selectivity coefficients; the pPD permselective layer is specifically implemented to prevent potential EBC electroactive interferents.

Dry-wet sensor stability test. Sensors were evaluated over multiple days in two modes. For dry-wet cycling, each day comprised a calibration test followed by transfer into aliquoted EBC and passive evaporation under ambient conditions; this cycle was repeated across days to emulate intermittent use. For in-EBCLite system continuous on-body wear, sensors were integrated into the mask and worn under natural breathing over multiple consecutive days, with a short calibration test at the start and end of each session. Across days and modes, the calibration and measurement responses were consistent within experimental uncertainty, with no systematic bias between the two protocols.

Perovskite precursor preparation

$\text{MBA}_2(\text{Cs}_{0.12}\text{MA}_{0.88})_6\text{Pb}_7\text{I}_{22}$ precursor solutions were prepared as described previously²⁶: 0.7 mmol PbI_2 , 1.18 mmol methylammonium iodide and 0.3 mmol PbCl_2 were dissolved together with 0.3 mmol methylbenzyl ammonium iodide in $660 \mu\text{l}$ DMF and $73 \mu\text{l}$ acetylacetone for 1 h at 62°C . Afterwards, $100 \mu\text{l}$ from a 1.5 M CsI solution in DMSO was added, and everything was left to mix for another 4 h at 62°C . The cloudy solution was then filtered through a $0.45\text{-}\mu\text{m}$ polytetrafluoroethylene filter before deposition.

Fabrication of ultralight flexible solar modules

FPSCs were fabricated on ultrathin $6\text{-}\mu\text{m}$ -thick PET substrates supported by glass. First, glass substrates measuring $35 \times 35\text{ mm}$ were thoroughly cleaned using sequential 15-min ultrasonic baths in a 2 vol% Hellmanex solution, followed by deionized water, acetone and IPA. Next, a PDMS adhesion layer was prepared by mixing PDMS base and curing agent in a 10:1 weight ratio, then diluting it with hexane at a 1:2 ratio. This mixture was spin-coated onto the cleaned glass at 4,000 revolutions per minute (rpm) for 30 s and thermally cured at 150°C for 15 min, allowing the attachment of the PET foil through van der Waals forces.

After the PET adhesion, the substrates were annealed at 115°C for 15 min. To enhance the barrier properties, a 100-nm layer of amorphous AlO_x was coated onto the PET foil using atomic layer deposition (ALD) with a Cambridge NanoTech Savannah 100 system. The ALD process used trimethylaluminum and ultrapure water as precursors, with nitrogen (N_2) as both the carrier and purge gas. Deposition was carried out at 125°C for 900 ALD cycles, achieving a growth rate of 1.11 \AA per cycle. The film thickness was verified using atomic force microscopy (Veeco Dimension 3100) and profilometry (Ambios-XP1).

Chromium/gold (Cr/Au) busbars ($10/100\text{ nm}$) were then thermally evaporated onto the AlO_x -coated PET using a shadow mask in a high-vacuum environment (-10^{-6} mbar). The chromium layer was used to improve gold adhesion.

For the HTL, the PEDOT:PSS was modified with 12 vol% DMSO and 0.7 vol% Zonyl surfactant, filtered through a 0.45- μm filter and spin-coated onto the PET/AlO₃ substrate at 1,500 rpm for 45 s. The film was subsequently annealed at 120 °C for 15 min, rinsed twice with IPA by spin-coating at 4,000 rpm for 15 s, and again annealed at 120 °C, resulting in a sheet resistance of approximately 105 $\Omega\text{ sq}^{-1}$.

In the P1 scribing process, individual cells of the module were divided by scribing 100- μm -thick traces into the conductive PEDOT:PSS films at the edges of the Cr/Au busbars using a fibre laser (Speedy 300, Trotec). Further processing was conducted in a nitrogen glovebox unless ambient conditions were needed.

The perovskite precursor solution was applied using a two-step spin-coating method: initially at 1,000 rpm for 5 s (with a ramp of 200 rpm s⁻¹), followed by 4,000 rpm for 25 s (with a ramp of 2,000 rpm s⁻¹). During the final 15 s of this step, 0.19 ml of chlorobenzene was dispensed at a rate of 95 $\mu\text{l s}^{-1}$ using an automated syringe for in situ antisolvent quenching. The films were then annealed at 100 °C for 1 h.

The PEAI quasi-2D interlayer was applied to the perovskite layer using dynamic spin-coating at 5,000 rpm for 30 s. After 5 s, 0.2 ml of PEAI (0.3% in a 1:200 DMF:IPA solution) was dispensed at 100 $\mu\text{l s}^{-1}$, and the layer was then annealed at 100 °C for 5 min.

After cooling, 75 nm of DiMe-PTCDI was thermally evaporated through a shadow mask in a high-vacuum environment ($\sim 10^{-6}$ mbar) at a rate of 0.1 \AA s^{-1} .

The P2 process for removing the entire HTL/perovskite/ETL stack to connect two adjacent cells in series involves ablating a 200- μm -thick trace directly over the Cr/Au bus bars. This is accomplished using laser parameters specifically set to avoid damaging the Cr/Au layers. To minimize the risk of shunting to the HTL across the P1 scribe, a thin layer of polystyrene (5 wt% in toluene) was manually applied using a brush. This additional manual step can introduce slight variations in the resulting active area across the tested FPSC modules.

Top contacts (Cr/Au 10/100 nm) were deposited by thermal evaporation under vacuum ($\sim 10^{-6}$ mbar) through a shadow mask.

To protect the FPSCs during bending and enhance their mechanical robustness, a superstrate of approximately 1–2 μm PU was applied. This was done by spin-coating 400 μl of filtered PU resin (CRC Kontakt Chemie Urethan 71) at 4,000 rpm for 33 s (with a ramp of 2,000 rpm s⁻¹). Contact areas were cleaned with a toluene-soaked cotton swab, and residual solvent was removed by heating the devices at 50 °C for 10 min. The PU layer helps shift the active region closer to the neutral mechanical plane, reducing stress during deformation and enhancing flexibility.

Small flexible solar cells were produced similarly to the module, but without the laser scribing process.

Characterization and evaluation of flexible solar modules

Details are provided in Supplementary Methods.

Circuit design

The electronic subsystem was designed for autonomous operation under variable ambient light by integrating efficient energy harvesting, low-power data acquisition and wireless communication modules. A flexible solar cell continuously harvested illumination, with energy regulated and stored by an ultralow-power power management integrated circuit (PMIC, BQ25570, Texas Instruments) featuring MPPT and programmable undervoltage/overvoltage thresholds. Harvested energy was buffered in a 5-mF capacitor and supplied to downstream electronics once the voltage surpassed a preset threshold. The PMIC maintained a stable 3-V output for system operation. A BLE-enabled microcontroller (CYBLE-222014, Infineon Technologies) handled wireless transmission, sensing coordination and system control. Electrochemical sensing was enabled by a multifunctional analogue front end (AD5941, Analog Devices), which supported both impedance and d.c. electrochemical modes with selectable gain paths and

onboard waveform generation. Built-in sequencing and hardware-level protocol execution reduced microcontroller load and power consumption. A switch matrix and multiplexer provided flexible sensor-channel routing.

System integration

The EBCLite system was fabricated by sequentially integrating the biosensing, condensation, microfluidic, sunshield and energy harvesting layers using biocompatible silicone adhesive. An ultrathin flexible solar cell was conformally adhered to the outer surface of the sunshield to provide a low-profile energy-harvesting interface, and a cooling hydrogel was subsequently laminated onto the backside to complete the multilayer architecture. A FPCB was mounted on the inner surface of the sunshield using double-sided adhesive, with electrical interconnections to the biosensor and solar cell established via anisotropic conductive film, enabling vertical conduction while maintaining lateral insulation. To interface with the user, a circular aperture was laser-cut into a commercial N95 respirator (3M 9205+), and the assembled sensing module was affixed using medical tape. Final wiring was completed to yield a fully integrated, self-powered wearable platform.

On-body evaluation of the wearable device

The validation and evaluation of the smart mask system were conducted with human participants in accordance with ethical guidelines under approved protocols (IR22-1278 and IR19-0892) by the Institutional Review Board at the California Institute of Technology. Healthy volunteers aged 18 and above were recruited from the Caltech campus and surrounding communities. Written informed consent was obtained from all participants before enrolment. The carbohydrate intake study included three participants (#1–3), and the exercise challenge included ten participants (#1–10). Participant details are provided in Supplementary Table 7. All human studies were conducted under approved protocols with appropriate permissions, and participants were compensated at a rate of US\$25 per hour.

Carbohydrate intake studies

Participants arrived at the laboratory after overnight fasting. The EBCLite system was mounted and calibrated at rest. On separate days, participants consumed standardized meals containing approximately 1 g kg⁻¹ and 2 g kg⁻¹ body weight of digestible carbohydrates, respectively. Standardized carbohydrate sources included high-carbohydrate solid foods (bread, rice and energy bars). Participants remained seated indoors under standard laboratory lighting throughout the 4-h test. EBC samples were automatically collected, and lactate signals were recorded continuously. pH and temperature data were simultaneously acquired and used as real-time references for lactate signal calibration. Blood samples were obtained at regular intervals for parallel lactate measurements.

Exercise challenge studies

To evaluate exercise-induced metabolic responses, participants performed constant-load cycling on a stationary ergometer. Exercise intensity was progressively increased using a stepwise ramp protocol during each session. The participant was continuously monitored indoors under standard laboratory lighting. EBC lactate levels were recorded dynamically throughout the exercise and recovery phases. Blood lactate samples were collected periodically for comparison. Across on-body tests performed on participants of different ages, exercise workloads were not fully standardized owing to interindividual variations in physical fitness.

Daily living wear test

A 4-day free-living trial was conducted to assess the system's long-term performance. The participant wore the EBCLite mask from morning to evening under alternating ambient conditions: outdoor sunlight, indoor laboratory lighting and room lighting. Physical activity, food

intake and rest periods were unstructured but logged. The device recorded exhaled lactate, pH and temperature continuously. The integrated flexible solar cell maintained stable power supply throughout the trial, regardless of lighting conditions.

Simulated inhaled aerosol ion quantification

Inhalation exposure to aerosolized ions was simulated using a vacuum-assisted set-up comprising a three-dimensionally printed facial mould conformally sealed inside a standard mask, continuous suction to reproduce inspiratory flow and a dedicated downstream collection chamber; the polymer-based EBCLite module was kept physically isolated from the vacuum outlet to prevent artificial entrainment. Inner mould and chamber surfaces were rinsed with deionized water at 1-h intervals to recover deposited aerosols, and the rinsates were analysed for target ions (for example, Li⁺) by ICP-MS with external calibration.

In vitro biocompatibility assessment

The cytotoxicity of the device was evaluated using Calu-3 human airway epithelial cells (HTB-55, ATCC) cultured in Eagle's Minimum Essential Medium supplemented with 10% horse serum at 37 °C and 5% CO₂. Cells at passages 3–5 were used, subcultured at ~70% confluency to ensure consistency. Device extracts were prepared following ISO 10993-5 protocols and applied to cell cultures for 24 h. Metabolic activity was quantified by 3-(4,5-dimethylthiazol-2-yl)-2,5-diphenyltetrazolium bromide (MTT) assay, measuring formazan absorbance at 570 nm. In parallel, cell viability and membrane integrity were assessed by live/lead staining with Calcein-AM and ethidium homodimer-1, followed by fluorescence microscopy. A high density of viable cells with minimal red fluorescence was observed in both control and extract-treated groups, indicating negligible cytotoxicity.

Statistics and reproducibility

Sample sizes were selected based on experience from previous wearable sensor studies and practical considerations of participant availability. All experiments were independently repeated as indicated in the figure legends, and representative results are shown. No data were excluded from the analyses. The experiments were not randomized, and the investigators were not blinded to allocation during experiments and outcome assessment.

Reporting summary

Further information on research design is available in the Nature Portfolio Reporting Summary linked to this article.

Data availability

The main data supporting the results of this study are available within the article and its Supplementary Information. Source data are provided with this paper.

References

- Heng, W. et al. A smart mask for exhaled breath condensate harvesting and analysis. *Science* **385**, 954–961 (2024).
- Horváth, I., Hunt, J. & Barnes, P. J. Exhaled breath condensate: methodological recommendations and unresolved questions. *Eur. Respir. J.* **26**, 523–548 (2005).
- Heng, W., Yin, S., Chen, Y. & Gao, W. Exhaled breath analysis: from laboratory test to wearable sensing. *IEEE Rev. Biomed. Eng.* **18**, 50–73 (2024).
- Fahy, J. V. & Dickey, B. F. Airway mucus function and dysfunction. *N. Engl. J. Med.* **363**, 2233–2247 (2010).
- Ma, J. et al. Airborne biomarker localization engine for open-air point-of-care detection. *Nat. Chem. Eng.* **2**, 321–333 (2025).
- Li, X. et al. Rapid and on-site wireless immunoassay of respiratory virus aerosols via hydrogel-modulated resonators. *Nat. Commun.* **15**, 4035 (2024).
- Li, H. et al. Wireless, battery-free, multifunctional integrated bioelectronics for respiratory pathogens monitoring and severity evaluation. *Nat. Commun.* **14**, 7539 (2023).
- Brasier, N. et al. Applied body-fluid analysis by wearable devices. *Nature* **636**, 57–68 (2024).
- Kim, J., Campbell, A. S., de Ávila, B. E.-F. & Wang, J. Wearable biosensors for healthcare monitoring. *Nat. Biotechnol.* **37**, 389–406 (2019).
- Yang, Y. et al. A laser-engraved wearable sensor for sensitive detection of uric acid and tyrosine in sweat. *Nat. Biotechnol.* **38**, 217–224 (2020).
- Ates, H. C. & Dincer, C. Wearable breath analysis. *Nat. Rev. Bioeng.* **1**, 80–82 (2023).
- Nguyen, P. Q. et al. Wearable materials with embedded synthetic biology sensors for biomolecule detection. *Nat. Biotechnol.* **39**, 1366–1374 (2021).
- Maier, D. et al. Toward continuous monitoring of breath biochemistry: a paper-based wearable sensor for real-time hydrogen peroxide measurement in simulated breath. *ACS Sens.* **4**, 2945–2951 (2019).
- Wang, R., Du, Y., Wan, X., Xu, J. & Chen, J. On-mask magnetoelastic sensor network for self-powered respiratory monitoring. *ACS Nano* **19**, 26862–26870 (2025).
- Maranhao, B. et al. Probability of fit failure with reuse of N95 mask respirators. *Br. J. Anaesth.* **125**, e322–e324 (2020).
- Lai, C. & Lu, L. Hydrogel-based thermal regulation strategies for passive cooling: a review. *Energy Built Environ.* <https://doi.org/10.1016/j.enbenv.2024.10.002> (2024).
- Wang, M. et al. Printable molecule-selective core–shell nanoparticles for wearable and implantable sensing. *Nat. Mater.* **24**, 589–598 (2025).
- Gao, M. et al. Power generation for wearable systems. *Energy Environ. Sci.* **14**, 2114–2157 (2021).
- Fan, X. et al. Flexible and wearable power sources for next-generation wearable electronics. *Batteries Supercaps* **3**, 1262–1274 (2020).
- Bravo Diaz, L. et al. Review—meta-review of fire safety of lithium-ion batteries: industry challenges and research contributions. *J. Electrochem. Soc.* **167**, 090559 (2020).
- Park, C. et al. Adaptive electronics for photovoltaic, photoluminescent and photometric methods in power harvesting for wireless wearable sensors. *Nat. Commun.* **16**, 5808 (2025).
- Song, Y. et al. Wireless battery-free wearable sweat sensor powered by human motion. *Sci. Adv.* **6**, eaay9842 (2020).
- Kishore, R. A., Nozariasbmarz, A., Poudel, B., Sanghadasa, M. & Priya, S. Ultra-high performance wearable thermoelectric coolers with less materials. *Nat. Commun.* **10**, 1765 (2019).
- Min, J. et al. An autonomous wearable biosensor powered by a perovskite solar cell. *Nat. Electron.* **6**, 630–641 (2023).
- Kaltenbrunner, M. et al. Flexible high power-per-weight perovskite solar cells with chromium oxide–metal contacts for improved stability in air. *Nat. Mater.* **14**, 1032–1039 (2015).
- Hailegnaw, B. et al. Flexible quasi-2D perovskite solar cells with high specific power and improved stability for energy-autonomous drones. *Nat. Energy* **9**, 677–690 (2024).
- Kantareddy, S. N. R. et al. Perovskite PV-powered RFID: enabling low-cost self-powered IoT sensors. *IEEE Sens. J.* **20**, 471–478 (2020).
- Han, W. et al. All irradiance-applicable, perovskite solar cells-powered flexible self-sustaining sensor nodes for wireless internet-of-things. *Adv. Funct. Mater.* **35**, 2425697 (2025).
- Best research-cell efficiency chart. NREL <https://www.nrel.gov/pv/cell-efficiency> (2025).
- Culik, P. et al. Design and cost analysis of 100 MW perovskite solar panel manufacturing process in different locations. *ACS Energy Lett.* **7**, 3039–3044 (2022).

31. He, X. et al. 40.1% record low-light solar-cell efficiency by holistic trap-passivation using micrometer-thick perovskite film. *Adv. Mater.* **33**, 2100770 (2021).
32. Zhang, J., Zhang, W., Cheng, H.-M. & Silva, S. R. P. Critical review of recent progress of flexible perovskite solar cells. *Mater. Today* **39**, 66–88 (2020).
33. Shirayama, M. et al. Degradation mechanism of $\text{CH}_3\text{NH}_3\text{PbI}_3$ perovskite materials upon exposure to humid air. *J. Appl. Phys.* **119**, 115501 (2016).
34. Kore, P. B., Jamshidi, M. & Gardner, M. J. The impact of moisture on the stability and degradation of perovskites in solar cells. *Mater. Adv.* **5**, 2200–2217 (2024).
35. Mikkelsen, M. E. et al. Serum lactate is associated with mortality in severe sepsis independent of organ failure and shock. *Crit. Care Med.* **37**, 1670–1677 (2009).
36. Ouyang, J., Wang, H. & Huang, J. The role of lactate in cardiovascular diseases. *Cell Commun. Signal.* **21**, 317 (2023).
37. Hirschhaeuser, F., Sattler, U. G. A. & Mueller-Klieser, W. Lactate: a metabolic key player in cancer. *Cancer Res.* **71**, 6921–6925 (2011).
38. Chen, H. et al. NBS1 lactylation is required for efficient DNA repair and chemotherapy resistance. *Nature* **631**, 663–669 (2024).
39. Kraut, J. A. & Madias, N. E. Lactic acidosis. *N. Engl. J. Med.* **371**, 2309–2319 (2014).
40. Beneke, R., Leithäuser, R. M. & Ochentel, O. Blood lactate diagnostics in exercise testing and training. *Int. J. Sports Physiol. Perform.* **6**, 8–24 (2011).
41. Spurway, N. C. Aerobic exercise, anaerobic exercise and the lactate threshold. *Br. Med. Bull.* **48**, 569–591 (1992).
42. Poole, D. C., Burnley, M., Vanhatalo, A., Rossiter, H. B. & Jones, A. M. Critical power: an important fatigue threshold in exercise physiology. *Med. Sci. Sports Exerc.* **48**, 2320–2334 (2016).
43. Leija, R. G. et al. Enteric and systemic postprandial lactate shuttle phases and dietary carbohydrate carbon flow in humans. *Nat. Metab.* **6**, 670–677 (2024).
44. Rabinowitz, J. D. & Enerbäck, S. Lactate: the ugly duckling of energy metabolism. *Nat. Metab.* **2**, 566–571 (2020).
45. Toffaletti, J. G. Blood lactate: biochemistry, laboratory methods, and clinical interpretation. *Crit. Rev. Clin. Lab. Sci.* **28**, 253–268 (1991).
46. Gao, W. et al. Fully integrated wearable sensor arrays for multiplexed in situ perspiration analysis. *Nature* **529**, 509–514 (2016).
47. Kim, J. et al. Non-invasive mouthguard biosensor for continuous salivary monitoring of metabolites. *Analyst* **139**, 1632–1636 (2014).
48. Tehrani, F. et al. An integrated wearable microneedle array for the continuous monitoring of multiple biomarkers in interstitial fluid. *Nat. Biomed. Eng.* **6**, 1214–1224 (2022).
49. Arwani, R. T. et al. Stretchable ionic–electronic bilayer hydrogel electronics enable in situ detection of solid-state epidermal biomarkers. *Nat. Mater.* **23**, 1115–1122 (2024).
50. Zhang, S. et al. Rapid measurement of lactate in the exhaled breath condensate: biosensor optimization and in-human proof of concept. *ACS Sens.* **7**, 3809–3816 (2022).
51. Lillis, B., Grogan, C., Berney, H. & Lane, W. A. Investigation into immobilisation of lactate oxidase to improve stability. *Sens. Actuators B* **68**, 109–114 (2000).
52. Minagawa, H., Nakayama, N., Matsumoto, T. & Ito, N. Development of long life lactate sensor using thermostable mutant lactate oxidase. *Biosens. Bioelectron.* **13**, 313–318 (1998).
53. Zhou, L. et al. Highly efficient and stable planar perovskite solar cells with modulated diffusion passivation toward high power conversion efficiency and ultrahigh fill factor. *Sol. RRL* **3**, 1900293 (2019).
54. Jiang, Q. et al. Surface passivation of perovskite film for efficient solar cells. *Nat. Photon.* **13**, 460–466 (2019).
55. Hamadani, B. H. Understanding photovoltaic energy losses under indoor lighting conditions. *Appl. Phys. Lett.* **117**, 043904 (2020).
56. Qamar, M. Z. et al. Advancement in indoor energy harvesting through flexible perovskite photovoltaics for self-powered IoT applications. *Nano Energy* **129**, 109994 (2024).
57. Khenkin, M. V. et al. Consensus statement for stability assessment and reporting for perovskite photovoltaics based on ISOS procedures. *Nat. Energy* **5**, 35–49 (2020).
58. Strawbridge, R. & Young, A. H. Lithium: how low can you go? *J. Bipolar Disord.* **12**, 4 (2024).
59. Reaven, G. M., Hollenbeck, C., Jeng, C.-Y., Wu, M. S. & Chen, Y.-D. I. Measurement of plasma glucose, free fatty acid, lactate, and insulin for 24 h in patients with NIDDM. *Diabetes* **37**, 1020–1024 (1988).
60. Hailegnaw, B. et al. Inverted (p–i–n) perovskite solar cells using a low temperature processed TiO_x interlayer. *RSC Adv.* **8**, 24836–24846 (2018).
61. De France, K. J., Xu, F. & Hoare, T. Structured macroporous hydrogels: progress, challenges, and opportunities. *Adv. Healthc. Mater.* **7**, 1700927 (2018).

Acknowledgements

This work was supported through the Heritage Medical Research Institute (W.G.), the Horizon 2020 research and innovation programme of the European Union under grant agreement number 101016411 ‘Soft Milli-robots-SOMIRO’ (M.K.). The funders had no role in the study design, data collection and analysis, decision to publish or preparation of the manuscript. We acknowledge N. Dalleska for help with ICP-MS.

Author contributions

W.G., M.K., W.H. and C.P. initiated the concept and designed the studies; W.H., C.P. and W.T. led the experiments and collected the overall data; W.H., W.T., J.M., G.K., C.W., M.-J.K. and Y.C. contributed to EBCLite characterization, validation and sample analysis. C.P., L.E.L., B.H., S.D. and M.S. contributed to solar module development, fabrication and characterization. C.P. and E.R. contributed to experimental design and characterization of VOC test for the solar module. W.G., M.K. and Z.F. supervised the studies. W.H., C.P., L.E.L., W.G. and M.K. cowrote the paper. All authors contributed to the data analysis and provided the feedback on the paper.

Competing interests

The authors declare no competing interests.

Additional information

Supplementary information The online version contains supplementary material available at <https://doi.org/10.1038/s44460-026-00041-3>.

Correspondence and requests for materials should be addressed to Zhiyong Fan, Martin Kaltenbrunner or Wei Gao.

Peer review information *Nature Sensors* thanks Jingcheng Ma and the other, anonymous, reviewer(s) for their contribution to the peer review of this work.

Reprints and permissions information is available at www.nature.com/reprints.

Publisher’s note Springer Nature remains neutral with regard to jurisdictional claims in published maps and institutional affiliations.

Springer Nature or its licensor (e.g. a society or other partner) holds exclusive rights to this article under a publishing agreement with the author(s) or other rightsholder(s); author self-archiving of the accepted manuscript version of this article is solely governed by the terms of such publishing agreement and applicable law.

© The Author(s), under exclusive licence to Springer Nature Limited 2026

Reporting Summary

Nature Portfolio wishes to improve the reproducibility of the work that we publish. This form provides structure for consistency and transparency in reporting. For further information on Nature Portfolio policies, see our [Editorial Policies](#) and the [Editorial Policy Checklist](#).

Statistics

For all statistical analyses, confirm that the following items are present in the figure legend, table legend, main text, or Methods section.

- | n/a | Confirmed |
|-------------------------------------|--|
| <input type="checkbox"/> | <input checked="" type="checkbox"/> The exact sample size (n) for each experimental group/condition, given as a discrete number and unit of measurement |
| <input type="checkbox"/> | <input checked="" type="checkbox"/> A statement on whether measurements were taken from distinct samples or whether the same sample was measured repeatedly |
| <input checked="" type="checkbox"/> | <input type="checkbox"/> The statistical test(s) used AND whether they are one- or two-sided
<i>Only common tests should be described solely by name; describe more complex techniques in the Methods section.</i> |
| <input checked="" type="checkbox"/> | <input type="checkbox"/> A description of all covariates tested |
| <input checked="" type="checkbox"/> | <input type="checkbox"/> A description of any assumptions or corrections, such as tests of normality and adjustment for multiple comparisons |
| <input type="checkbox"/> | <input checked="" type="checkbox"/> A full description of the statistical parameters including central tendency (e.g. means) or other basic estimates (e.g. regression coefficient) AND variation (e.g. standard deviation) or associated estimates of uncertainty (e.g. confidence intervals) |
| <input type="checkbox"/> | <input checked="" type="checkbox"/> For null hypothesis testing, the test statistic (e.g. F , t , r) with confidence intervals, effect sizes, degrees of freedom and P value noted
<i>Give P values as exact values whenever suitable.</i> |
| <input checked="" type="checkbox"/> | <input type="checkbox"/> For Bayesian analysis, information on the choice of priors and Markov chain Monte Carlo settings |
| <input checked="" type="checkbox"/> | <input type="checkbox"/> For hierarchical and complex designs, identification of the appropriate level for tests and full reporting of outcomes |
| <input type="checkbox"/> | <input checked="" type="checkbox"/> Estimates of effect sizes (e.g. Cohen's d , Pearson's r), indicating how they were calculated |

Our web collection on [statistics for biologists](#) contains articles on many of the points above.

Software and code

Policy information about [availability of computer code](#)

Data collection

Data analysis

For manuscripts utilizing custom algorithms or software that are central to the research but not yet described in published literature, software must be made available to editors and reviewers. We strongly encourage code deposition in a community repository (e.g. GitHub). See the Nature Portfolio [guidelines for submitting code & software](#) for further information.

Data

Policy information about [availability of data](#)

All manuscripts must include a [data availability statement](#). This statement should provide the following information, where applicable:

- Accession codes, unique identifiers, or web links for publicly available datasets
- A description of any restrictions on data availability
- For clinical datasets or third party data, please ensure that the statement adheres to our [policy](#)

Data availability

Research involving human participants, their data, or biological material

Policy information about studies with [human participants or human data](#). See also policy information about [sex, gender \(identity/presentation\), and sexual orientation](#) and [race, ethnicity and racism](#).

Reporting on sex and gender	Sex and gender were not considered in the study.
Reporting on race, ethnicity, or other socially relevant groupings	These information were not considered in the study.
Population characteristics	Healthy individuals between the ages of 18 and 65 with body mass index (BMI) of 18.5 to 24.9 kg m ⁻² .
Recruitment	The healthy participants were recruited from both the Caltech campus and nearby communities around Los Angeles, California. All study participants provided written informed consent prior to their involvement in the research.
Ethics oversight	Institutional Review Board (IRB) at the California Institute of Technology

Note that full information on the approval of the study protocol must also be provided in the manuscript.

Field-specific reporting

Please select the one below that is the best fit for your research. If you are not sure, read the appropriate sections before making your selection.

Life sciences Behavioural & social sciences Ecological, evolutionary & environmental sciences

For a reference copy of the document with all sections, see [nature.com/documents/nr-reporting-summary-flat.pdf](https://www.nature.com/documents/nr-reporting-summary-flat.pdf)

Life sciences study design

All studies must disclose on these points even when the disclosure is negative.

Sample size	For on body evaluation of the complete wearable smart mask, 10 healthy subjects were recruited. For on body validation of the carbohydrate intake, 3 healthy subjects were recruited. For on body validation of the exercise, 10 healthy subjects were recruited.
Data exclusions	No data exclusion.
Replication	Three users were asked to perform the sensors independently. All attempts at replication were successful when following the device fabrication process described in the paper.
Randomization	The device was fabricated with same process and was tested in all participants under same conditions. Randomization was therefore not relevant to the study.
Blinding	Not relevant, because a blinding process wouldn't influence the sampling result.

Reporting for specific materials, systems and methods

We require information from authors about some types of materials, experimental systems and methods used in many studies. Here, indicate whether each material, system or method listed is relevant to your study. If you are not sure if a list item applies to your research, read the appropriate section before selecting a response.

Materials & experimental systems

n/a	Involved in the study
<input checked="" type="checkbox"/>	<input type="checkbox"/> Antibodies
<input type="checkbox"/>	<input checked="" type="checkbox"/> Eukaryotic cell lines
<input checked="" type="checkbox"/>	<input type="checkbox"/> Palaeontology and archaeology
<input checked="" type="checkbox"/>	<input type="checkbox"/> Animals and other organisms
<input checked="" type="checkbox"/>	<input type="checkbox"/> Clinical data
<input checked="" type="checkbox"/>	<input type="checkbox"/> Dual use research of concern
<input checked="" type="checkbox"/>	<input type="checkbox"/> Plants

Methods

n/a	Involved in the study
<input checked="" type="checkbox"/>	<input type="checkbox"/> ChIP-seq
<input checked="" type="checkbox"/>	<input type="checkbox"/> Flow cytometry
<input checked="" type="checkbox"/>	<input type="checkbox"/> MRI-based neuroimaging

Eukaryotic cell lines

Policy information about [cell lines and Sex and Gender in Research](#)

Cell line source(s)	Cytotoxicity of the device was evaluated using Calu-3 human airway epithelial cells HTB-55™
Authentication	All cells were purchased from ATCC and have been ethically sourced and authenticated by QC testing at ATCC.
Mycoplasma contamination	We confirm that all cell lines tested negative for mycoplasma contamination.
Commonly misidentified lines (See ICLAC register)	N/A

Plants

Seed stocks	<i>Report on the source of all seed stocks or other plant material used. If applicable, state the seed stock centre and catalogue number. If plant specimens were collected from the field, describe the collection location, date and sampling procedures.</i>
Novel plant genotypes	<i>Describe the methods by which all novel plant genotypes were produced. This includes those generated by transgenic approaches, gene editing, chemical/radiation-based mutagenesis and hybridization. For transgenic lines, describe the transformation method, the number of independent lines analyzed and the generation upon which experiments were performed. For gene-edited lines, describe the editor used, the endogenous sequence targeted for editing, the targeting guide RNA sequence (if applicable) and how the editor was applied.</i>
Authentication	<i>Describe any authentication procedures for each seed stock used or novel genotype generated. Describe any experiments used to assess the effect of a mutation and, where applicable, how potential secondary effects (e.g. second site T-DNA insertions, mosaicism, off-target gene editing) were examined.</i>